NANO LETTERS

pubs.acs.org/NanoLett Letter

Local Electronic Properties of Coherent Single-Layer WS_2/WSe_2 Lateral Heterostructures

Charlotte Herbig, Canxun Zhang, Fauzia Mujid, Saien Xie, Zahra Pedramrazi, Jiwoong Park,* and Michael F. Crommie*

Cite This: https://dx.doi.org/10.1021/acs.nanolett.0c04204 Read Online

ACCESS | Metrics & More | Article Recommendations | Supporting Information

ABSTRACT: Lateral single-layer transition metal dichalcogenide (TMD) heterostructures are promising building blocks for future ultrathin devices. Recent advances in the growth of coherent heterostructures have improved the structural precision of lateral heterojunctions, but an understanding of the electronic effects of the chemical transition at the interface and associated strain is lacking. Here we present a scanning tunneling microscopy study of single-layer coherent TMD heterostructures with nearly uniform strain on each side of the heterojunction interface. We have characterized the local topography and electronic structure of single-layer WS_2/WSe_2 heterojunctions exhibiting ultrasharp coherent interfaces. Uniform built-in strain on each side of the interface arising from lattice mismatch results in a reduction of the bandgap of WS_2. By mapping the tunneling differential conductance across the interface, we find type-II band alignment and an ultranarrow electronic transition region only ~3 nm in width that arises from wave function mixing between the two materials.

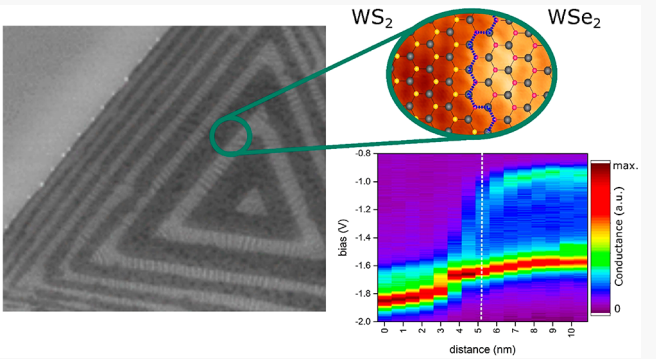

KEYWORDS: *Transition metal dichalcogenides, scanning tunneling microscopy, semiconductor heterostructures, strain engineering, wave function hybridization*

Semiconductor heterostructures (HSs) are composed of two different semiconducting materials that make contact at a junction interface. While most heterojunctions in van der Waals materials occur in the vertical (out-of-plane) direction, a number of atomically flat lateral heterojunctions have also been characterized.[1−7] For example, WS_2/WSe_2 and $MoSe_2/WSe_2$ heterojunctions made using chemical vapor deposition (CVD) techniques have been observed to exhibit diode-like responses and photovoltaic effects.[2,4,6] Lattice-mismatched in-plane HSs have also been shown to provide a platform for altering TMD electronic structure by means of strain engineering.[8−11] Irregular $MoSe_2/WSe_2$ interfaces have been observed to exhibit type-II band alignments and narrow transition regions, but this system does not allow intrinsic strain engineering due to the nearly identical lattice constants of TMDs with the same chalcogen atoms (i.e., Se in $MoSe_2$ and WSe_2).[12] HSs of WSe_2/MoS_2, on the other hand, have a lattice mismatch of approximately 4% (sulfides smaller than selenides) which has resulted in strong spatial variation in the electronic structure of MoS_2 caused by the irregular interface strain field.[7] Recently Li et al.[3] and Xie et al.[10] have shown that it is possible to fabricate lateral heterojunctions between different TMD materials that are defect-free despite large lattice mismatches. These "coherent" interfaces are grown using two-step CVD or metal−organic chemical vapor deposition (MOCVD) and have been shown to exhibit uniform strain distributions on either side of the heterojunction.[10] Although the electronic effects of such strain have been investigated using photoluminescence, the limited spatial resolution of this technique has not allowed the local, nanoscale interplay of interface electronic structure and strain effects to be investigated yet for coherent heterojunctions.

Here we present a combined synthesis and scanning tunneling microscopy/spectroscopy (STM/STS) characterization study of single-layer WS_2/WSe_2 lateral HSs with coherent interfaces more than 50 nm in length. Atomic-scale characterization via STM/STS allows us to identify both the effects of lattice-mismatch-induced nearly uniform strain and the effects of "wavefunction tailing"[13,14] across the interface. At large distances from the interface ($|\Delta x| > 1.5$ nm) we identify a strain-induced reduction of the bandgap in WS_2 by 240 meV, as well as a charge-transfer-induced rigid band shift on each side of the heterojunction. In the near-field region ($|\Delta x| \lesssim 1.5$

Received: October 21, 2020
Revised: March 6, 2021

https://dx.doi.org/10.1021/acs.nanolett.0c04204
Nano Lett. XXXX, XXX, XXX−XXX

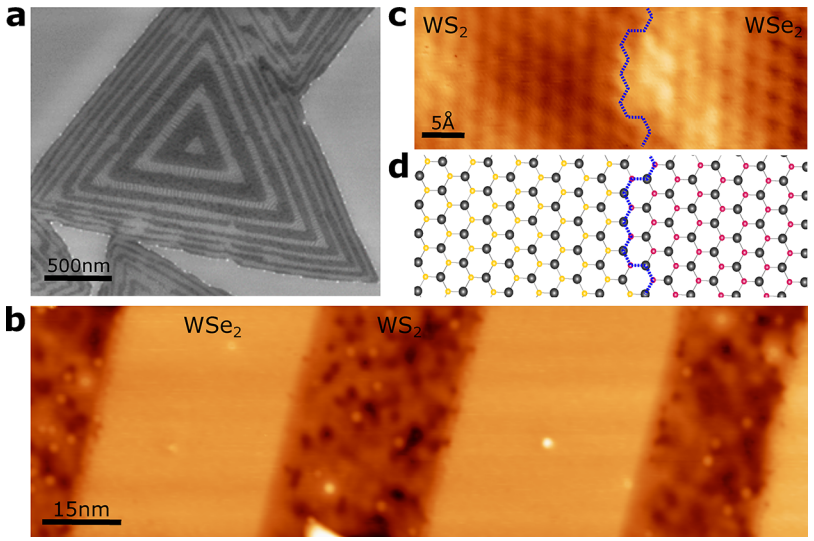

Figure 1. Lateral heterostructure of single-layer TMD. (a) SEM image of a coherent single-layer WS_2/WSe_2 superlattice on SiO_2. (b) Large-scale STM topograph of a coherent single-layer WS_2/WSe_2 superlattice after transfer from SiO_2 to graphite (HOPG). Scanning parameters: 10 pA, −1.8 V, T = 4.7 K. (c) Atomically resolved STM image of the coherent single-layer WS_2/WSe_2 interface (marked by dashed blue line). Scanning parameters: 50 pA, 1.5 V, T = 4.7 K. (d) Atomic model of the WS_2/WSe_2 heterojunction shown in (c). Tungsten atoms are black, sulfur atoms are yellow, and selenium atoms are pink. The interface is marked by a dashed blue line.

nm) we observe type-II band alignment and rapid electronic evolution arising from wave function mixing at the interface. We have spatially mapped these effects using dI/dV spectroscopy and are able to disentangle the effects of strain from our measurements to determine the intrinsic electronic length scale associated with wave function mixing between the two materials.

Coherent WS_2/WSe_2 superlattices were grown by modulated MOCVD on 300 nm SiO_2/Si wafers via the growth method previously reported in ref 10. At coherent interfaces the 4% lattice mismatch between WS_2 (a_0 = 0.315 nm) and WSe_2 (a_0 = 0.328 nm) is not released by dislocation defects; instead, nearly uniform strain is generated on each side of the heterojunction since the lattice constant parallel to the interface is held constant across the entire HS. Figure 1a displays an SEM image of a representative WS_2/WSe_2 superlattice with a large-scale triangular morphology and alternating stripes of dark and bright regions that correspond to WS_2 and WSe_2 single-layers, respectively (the width of the stripes is controlled by the growth time). To facilitate STM measurements, a modified growth procedure was adopted to ensure a high density and coverage of triangular WS_2/WSe_2 superlattices. This resulted in partial coalescence of the triangular islands and partial disruptions to straight interfaces at their outer edges compared to the well-separated superlattices in ref 10. Overall lattice coherency, however, was maintained. After growth and SEM characterization the triangular islands were transferred to highly oriented pyrolytic graphite (HOPG) using a water-assisted transfer method for STM/STS measurement (see Methods in the Supporting Information; a representative SEM image of transferred heterostructures on HOPG is shown in Figure S1).

A large-scale STM topograph of the transferred WS_2/WSe_2 HS is displayed in Figure 1b. The period of the WS_2/WSe_2 superlattice is approximately 70 nm with slightly wider WSe_2 regions. The origin of the topographic contrast between the two materials is mostly electronic due to different band offsets that provide a lower (higher) apparent height for WS_2 (WSe_2) at a sample bias of −1.8 V (see the Supporting Information and Figure S2 for bias-dependent measurements). However, an abrupt interface can be found that is independent of the bias and so indicates a sharp chemical transition. Depending on the tunneling conditions, irregular features in the form of bright or dark dots are visible on both TMD materials with largely uniform density, which we ascribe to the surface adsorbates introduced during the growth and transfer. Comparison of atomic-resolution images (Figure 1c) obtained over the same area at different biases suggests the atomic interface model displayed in Figure 1d. We identify a zigzag interface that is interrupted by short armchair segments (dashed blue line) consistent with previous reports.[10]

The WS_2/WSe_2 HS maintains lattice coherence over a length scale of at least 50 nm (~150 unit cells (Figure 2a). No misfit dislocation can be found along the interface (red dashed line in Figure 2b) in the filtered inverse fast Fourier transform (FFT) of the area shown in Figure 2a. In the inverse FFT procedure the WS_2 and WSe_2 Bragg peaks in one direction (marked by blue circles in the FFT in Figure 2c) are isolated and inverted. In an incoherent superlattice an additional atomic row would be expected on the WS_2 side of Figure 2b at least every 25 unit cells to compensate for the lattice mismatch. Previous studies of incoherent HSs report even higher defect densities.[7]

We now analyze the strain distribution in the WS_2/WSe_2 HS based on structural characterization. The FFT peaks in Figure 2c all exhibit "doublet" behavior due to contributions from the two different materials. Quantitative determination of atomic lattice values from the doublet separation is difficult since the Bragg peaks of WS_2 and WSe_2 are too close for the largest k-values. On the other hand, the HS forms a moiré pattern with the underlying HOPG lattice due to lattice misfit and a rotation angle of ~10°. The moiré pattern is reflected in the FFT as doublet peaks that form at smaller k-values in Figure 2c, and they typically show a larger separation between the WS_2 and WSe_2 signals since they originate from higher order Bragg peaks (see Figure 2d). Projecting this separation onto

https://dx.doi.org/10.1021/acs.nanolett.0c04204
Nano Lett. XXXX, XXX, XXX−XXX

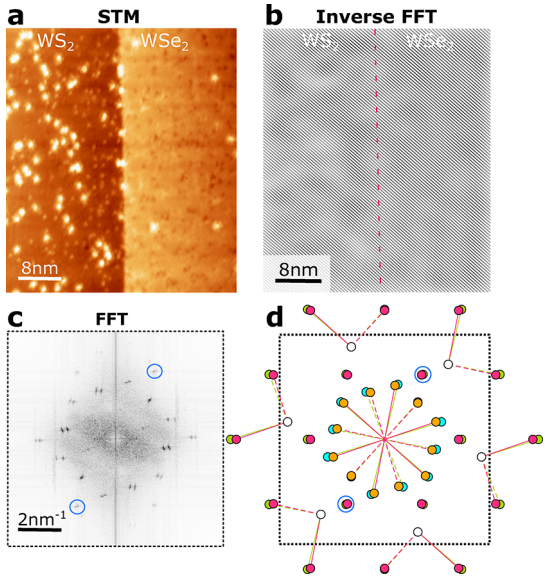

Figure 2. Coherent single-layer WS_2/WSe_2interface. (a) STM image of the coherent interface between WS_2 (left) and WSe_2 (right) for a single-layer heterojunction. Scanning parameters: 20 pA, −800 mV, T = 4.7 K. (b) Inverse FFT of area shown in (a) based on the two circled WS_2/WSe_2 Bragg peaks in the FFT shown in (c). Red dashed line indicates the position of the heterojunction interface. (c) FFT of the image shown in (a). (d) Color-coded graphical explanation of the FFT in (c). WS_2 Bragg peaks are green, WSe_2 Bragg peaks are pink, HOPG Bragg peaks are white, WS_2/HOPG moiré peaks are blue, WSe_2/HOPG moiré peaks are orange. The origin of the moiré peaks can be seen by the lines connecting TMD and HOPG Bragg peaks.

two orthogonal directions, we estimate the relative lattice mismatch between WS_2 and WSe_2 parallel to the interface to be

$$\frac{a_{\parallel}(WSe_2) - a_{\parallel}(WS_2)}{\bar{a}_{\parallel}} = (0.8 \pm 0.3)\% \quad (1)$$

and perpendicular to the interface to be

$$\frac{a_{\perp}(WSe_2) - a_{\perp}(WS_2)}{\bar{a}_{\perp}} = (3.7 \pm 0.4)\% \quad (2)$$

Previously reported coherent WS_2/WSe_2 superlattices grown by a similar method show a lattice mismatch close to zero along the interface and a lattice mismatch of 1.2% perpendicular to it.[10] We attribute the difference here to our slightly adjusted sample preparation procedures, including the growth recipe which yields a higher coverage to accommodate STM characterization as well as possible relaxation during the transfer to HOPG and annealing (including formation of some irregularities and cracks in the HS). Nevertheless, the lattice mismatch in the parallel direction in our sample is still much smaller than the pristine value of 4% (consistent with the coherent nature of the interface) and suggests a large mostly uniaxial built-in strain for both materials. No obvious rippling has been observed in our sample that could partially relax this strain (see the Supporting Information for details). The resulting parallel ($\varepsilon_{\parallel}$) and perpendicular ($\varepsilon_{\perp}$) components of the strain tensors for the two materials can be written as

$$\varepsilon_{\parallel,\perp}(WS_2) = \frac{a_{\parallel,\perp}(WS_2) - a_0(WS_2)}{a_0(WS_2)}$$

$$\varepsilon_{\parallel,\perp}(WSe_2) = \frac{a_{\parallel,\perp}(WSe_2) - a_0(WSe_2)}{a_0(WSe_2)} \quad (3)$$

Since $(a_0(WSe_2) - a_0(WS_2))/\bar{a}_0 = 4\%$, we have (to first order)

$$\varepsilon_{\parallel}(WS_2) - \varepsilon_{\parallel}(WSe_2) = 4\% - 0.8\% = 3.2\% \quad (4)$$

$$\varepsilon_{\perp}(WS_2) - \varepsilon_{\perp}(WSe_2) = 4\% - 3.7\% = 0.3\% \quad (5)$$

Both the atomic and moiré lattices remain uniform as one moves across the interface (Figure S3), consistent with an abrupt strain transition at the interface and also corroborating the uniformity of strain within each material.

After establishing the coherent nature of our TMD HS, we characterized the effects of the built-in mostly uniaxial strain on the band structure of WS_2 and WSe_2. To accomplish this, we first compared STS measurements that we acquired far (>7 nm) from the HS interface with STS measurements performed on pristine WS_2 and WSe_2 samples grown and transferred to HOPG in the same manner (i.e., "pure" single-layer WS_2 and WSe_2 without any heterojunctions). This ensures that the band renormalization effect from the substrate as well as possible artifacts in the gap determination procedure applies to both samples, and thus observed changes reflect the true difference between the HS and pristine single-layer TMD.[11] Figure 3b and Figure 3c show representative spectra of the valence and conduction bands of the HS obtained at the positions indicated by the green (WS_2) and pink (WSe_2) dots in the STM image in Figure 3a. In order to correctly identify the band edges, constant-height $(dI/dV)_Z$ spectra were taken over limited energy ranges. The position of the valence and conduction band onsets was determined by averaging over several spectra and utilizing the method established in ref 15. The conduction band minima (CBM) for WS_2 and WSe_2 are located at 0.64 and 1.15 eV above the Fermi level, whereas the valence band maxima (VBM) reside at −1.54 eV and −0.81 eV below the Fermi level, respectively (the bright or dark spots visible in the STM image had no noticeable effect on the STS). This results in a bandgap of 2.19 eV for WS_2 and 1.96 eV for WSe_2 in the heterostructure.

STS results for the pristine TMD single-layers are shown in Figure 3d,e. Here the CBM for WS_2 and WSe_2 are found at 0.91 and 1.16 eV while the VBM are found at −1.51 eV and −0.79 eV, yielding bandgaps of 2.42 and 1.95 eV for WS_2 and WSe_2, respectively. Our bandgap values agree well with some found in the literature,[16−19] but a larger bandgap of 2.12 eV for single-layer WSe_2 on HOPG has also been reported.[20] We attribute this discrepancy to the different methods utilized in determining band edge positions. Comparing our energy gap values for both the HS and pure materials, we deduce that WS_2 experiences a reduction in bandgap of 240 meV when it is incorporated into a coherent HS relative to a uniform material. The bandgap of WSe_2, on the other hand, is unchanged by incorporation into a coherent HS (see Table 1).

We next visualized the band structure across the coherent HS interface in order to map out the intrinsic length scale of the electronic transition. This is challenging due to the high dynamic range (several orders of magnitude) that is required in the tunnel current measurement to resolve all of the various features of the HS band structure. The problem is best

https://dx.doi.org/10.1021/acs.nanolett.0c04204
Nano Lett. XXXX, XXX, XXX−XXX

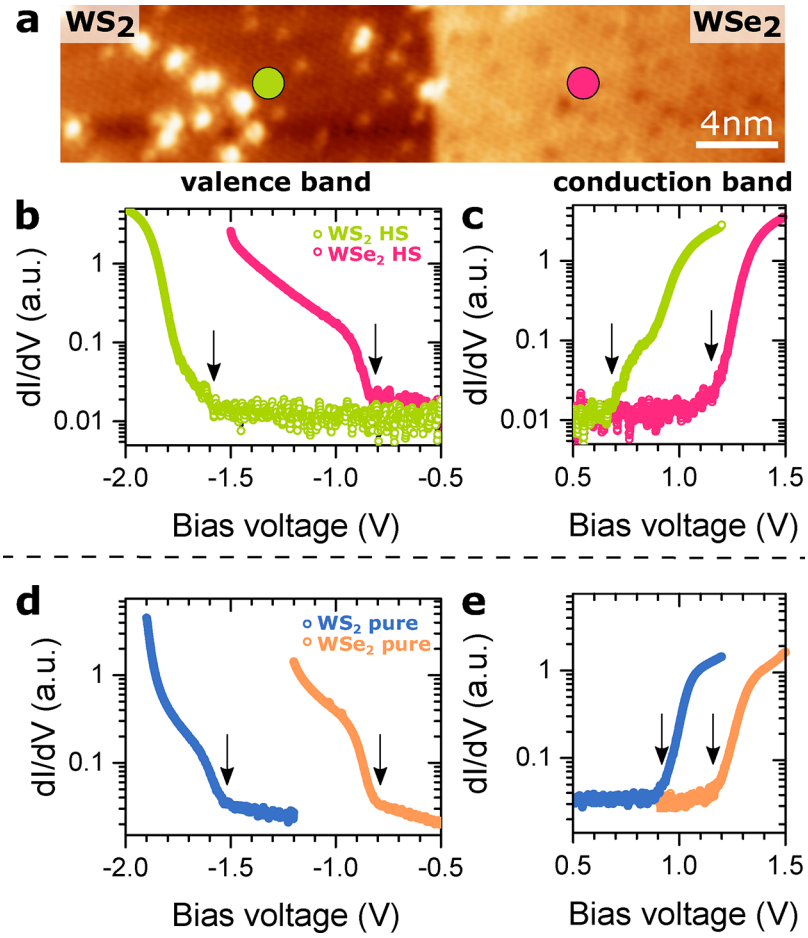

Figure 3. Determination of single-layer band edges. (a) STM image of the interface region of a coherent single-layer WS_2/WSe_2 heterojunction (WS_2 left; WSe_2 right; scanning parameters 20 pA, −800 mV). Constant-height STS spectra are shown for (b) valence bands (I_{set} = 100 pA, V_{mod} = 20 mV, WS_2 V_{set} = −2 V, WSe_2 V_{set} = −1.5 V) and (c) conduction bands (I_{set} = 100 pA, V_{mod} = 20 mV, WS_2 V_{set} = 1.2 V, WSe_2 V_{set} = 1.5 V) obtained in the WS_2 (green dot in (a)) and WSe_2 (pink dot in (a)) regions away from the interface. Constant-height STS spectra are also shown for (d) valence bands (I_{set} = 100 pA, V_{mod} = 20 mV, WS_2 V_{set} = −1.9 V, WSe_2 V_{set} = −1.2 V) and (e) conduction bands (I_{set} = 100 pA, V_{mod} = 20 mV, WS_2 V_{set} = 1.2 V, WSe_2 V_{set} = 1.5 V) of uniform single-layer WS_2 (blue curve) and uniform single-layer WSe_2 (orange curve) on HOPG. Black arrows indicate the positions of band edges. T = 4.7 K.

Table 1. Electronic Features: Conduction Band Minima (CBM), Valence Band Maxima (VBM), and Bandgap for Single-Layer WS_2/WSe_2 in Coherent HSs and Pure Single-Layer WS_2 and WSe_2

	CBM (eV)	VBM (eV)	bandgap (eV)
WS_2 (HS)	0.64	−1.54	2.19
WSe_2 (HS)	1.15	−0.81	1.96
WS_2 (pure)	0.91	−1.51	2.42
WSe_2 (pure)	1.16	−0.79	1.95

illustrated by looking at HS dI/dV spectra over the full energy range -2 V < V_b < 2 V shown in Figure 4a. Here a tip height was chosen to give a high dI/dV signal at the voltage end points (±2 V) and the tip was held at constant height during an open-feedback voltage scan. The problem occurs near the band edges where the dI/dV signal falls too low for detection. This reduction in signal strength is due to the fact that WS_2 and WSe_2 band edge states arise from the K- or Q-points of their respective band structures (see, for example, the band structures shown in ref 21). Band states with high parallel momentum, such as occur at the K-point, penetrate less into the vacuum than states that have low parallel momentum, such as occur at the Γ-point.[15] An STM tip must therefore be brought much closer to the surface to detect K/Q-point states. This is straightforward to accomplish but has the unfortunate side effect of then causing the dI/dV signal coming from the Γ-point states to rise too high, thus overloading the STM preamp. This can be seen from the dI/dV spectra of Figure 4b which were obtained at the same locations as in Figure 4a but with the tip brought closer to the surface by ∼1.6 Å. The filled-state spectrum taken on the WSe_2 side is now seen to have significant state density at V_b = −1 V that could not be seen in the spectrum of Figure 4a (marked by a vertical dashed line). Much of the Γ-point state density, however, is now lost, since the signal from the Γ-point states is too high for detection at a single gain setting (i.e., the signal for V_b < −1.5 V overloads the STM current preamp). A similar effect can be seen for conduction band states on the WS_2 side of the HS.

Such behavior has been noted before in single-layer TMDs,[15,22,23] and strategies have been developed to mitigate this issue and to increase the dynamic range of dI/dV sweeps.[15,16,20,24] One strategy explored by several groups involves keeping the feedback loop closed during dI/dV measurement so that the tip height changes during the voltage scan to keep the dc tunnel current constant.[7,20] States that do

https://dx.doi.org/10.1021/acs.nanolett.0c04204
Nano Lett. XXXX, XXX, XXX−XXX

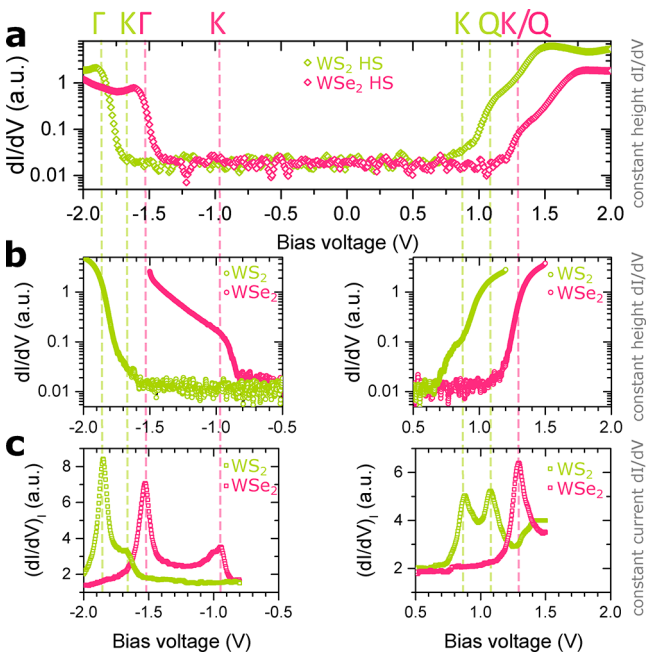

Figure 4. Comparison of constant-height and constant-current scanning tunneling spectroscopy. (a) Large-range constant-height dI/dV spectra obtained at the color-coded WS_2/WSe_2 HS positions shown in Figure 3a and plotted on a log scale (I_{set} = 100 pA, V_{set} = −2 V, V_{mod} = 20 mV). (b) Smaller energy range constant-height dI/dV spectra obtained for the same positions as (a) but with a smaller tip−surface separation (I_{set} = 100 pA, V_{mod} = 20 mV, WS_2 VB V_{set} = −2 V, WSe_2 VB V_{set} = −1.5 V, WS_2 CB V_{set} = 1.2 V, WSe_2 CB V_{set} = 1.5 V). (c) Constant-current dI/dV spectra from the same positions plotted on a linear scale (I_{set} = 10 pA, V_{mod} = 10 mV, VB V_{set} = −2 V, CB V_{set} = 1.5 V). Band-edge features in the spectra are marked by dashed lines that also indicate the band structure momenta identified with the marked states. T = 4.7 K.

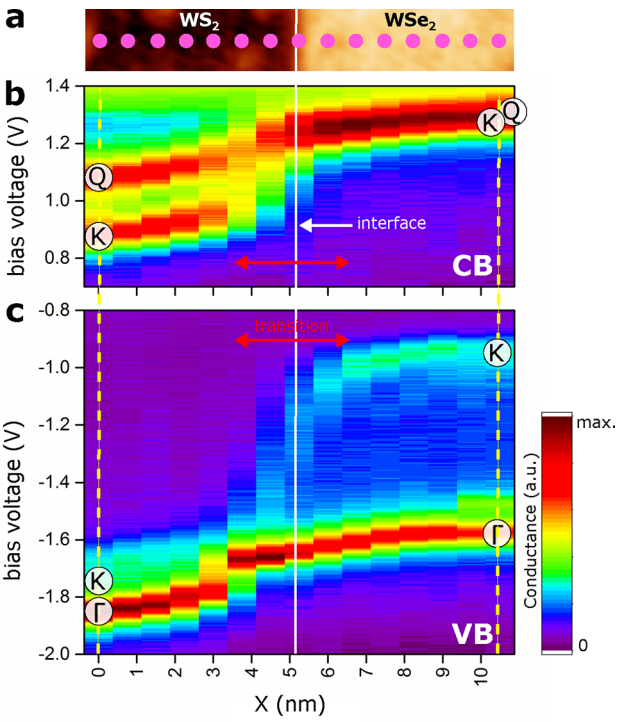

Figure 5. Heterojunction electronic structure evolution visualized by constant current spectroscopy. (a) STM topograph of coherent single-layer WS_2/WSe_2 interface (scanning parameters 20 pA, −800 mV, T = 4.7K). (b) and (c) show spatial dependence of constant-current dI/dV spectra of the CB and VB, respectively, obtained across the heterojunction interface along the trajectory marked by pink dots in (a). White line marks the interface, and red arrows indicate the near-field transition region. Yellow vertical dashed lines mark line-cuts corresponding to spectra shown in Figure 4c. Spectroscopy parameters: I_{set} = 10 pA, V_{mod} = 10 mV. T = 4.7 K.

not penetrate far into the vacuum are then detected as the tip naturally moves toward the surface. Quantitative analysis of such dI/dV spectra is complicated by convolution of the effects of tip motion, but states having very different vacuum penetration factors can be nicely observed in this way via a single dI/dV sweep. Zhang et al. have shown that this constant-current dI/dV technique ($(dI/dV)_I$) is effective for detecting K-point states in TMD layers that coexist with Γ-point states.[7,20] We have employed this technique to detect electronic states near the band edges in WS_2/WSe_2 HSs as shown in Figure 4c (the corresponding $(Z-V)_I$ curves are shown in Figure S4). Comparison of Figure 4c to Figure 4a,b shows that $(dI/dV)_I$ is effective at simultaneously detecting both K/Q-point and Γ-point band-edge states (which appear as resonances) over a wider range of energy than is possible with single-sweep constant-height dI/dV measurement.

We utilized this technique to map the evolution of single-layer WS_2/WSe_2 coherent HS electronic properties as a function of distance across the heterojunction interface (Figure 5). Figure 5b (empty states) and Figure 5c (filled states) show the result of constant current $(dI/dV)_I$ sweeps at different points along the trajectory shown in the STM topograph of Figure 5a (the HS interface lies at $x \approx 5$ nm). On the WS_2 side of the HS (left side) far from the interface (e.g., at x = 0) two distinct resonances are seen in the conduction band (empty states) that arise from states at the Q- and K-points of the WS_2 band structure. These can also be seen in the green spectrum of Figure 4c which corresponds to the yellow dashed line at x = 0 in Figure 5b (the filled states at x = 0 show a merged resonance arising from states at the Γ- and K-points that can also be seen in the green spectrum of Figure 4c). On the WSe_2 side of the HS (right side) far from the interface (e.g., at x = 10.5 nm) K- and Q-point states are seen to merge into a single resonance in the conduction band while the filled states show two widely separated resonances identified as K- and Γ-point states. These features are more clearly resolved in the pink spectra of Figure 4c.

Inspection of Figure 5 shows that the electronic states of WS_2 and WSe_2 smoothly merge as the interface is approached from either side. Two regimes can be identified with behavior near the interface ($|\Delta x| \lesssim 1.5$ nm) differing significantly from behavior far from the interface ($|\Delta x| > 1.5$ nm). In the far-field regime the rate of change of the electronic states is more gradual and the bandgap does not significantly change with position (i.e., the bands shift rigidly). In the near-field regime, however, a rapid merging of some states can be seen. On the WS_2 side, for example, the states associated with the K- and Q-points in the conduction band shift up sharply in the near-field region with the K-point states fully merging with the Q-point states as the interface is approached. The valence band states on the WSe_2 side exhibit an even more dramatic behavior. Here the states associated with the K- and Γ-points of the band structure which are strongly split in the far field regime quickly merge in the near-field region due to a fast collapse of the

https://dx.doi.org/10.1021/acs.nanolett.0c04204
Nano Lett. XXXX, XXX, XXX−XXX

energy of the K-point states. Overall, a type-II band alignment across the interface is observed.

An understanding of the physical origin of the interface behavior observed in coherent single-layer WS_2/WSe_2 HSs must begin with the effects of strain. Unlike a conventional lateral HS, the coherent interface in our HSs induces spatially uniform strain on each side of the junction (evidence supporting this arises from our observation of spatially uniform moiré patterns at different distances from the HS interface). Because WS_2 has a lattice constant 4% smaller than WSe_2, we expect the WS_2 to experience tensile strain and the WSe_2 to experience compressive strain. One of the most significant effects of the strain is to reduce the energy gap on the WS_2 side of the interface by 240 meV, as deduced from our measurements on "pure" single-layer WS_2 in the absence of a heterostructure. This gap reduction is also corroborated by comparing constant-current $(dI/dV)_I$ spectra obtained from both an HS (Figure 4c) and pristine WS_2 (Figure S5). We note that first-principle calculations indicate that strain-induced bandgap modification of TMD single-layers such as this is largely insensitive to strain anisotropy.[9] In other words, the change of energy gap is solely determined by the fractional area change $\Delta A/A$ (defined as the trace of the two-dimensional strain tensor). This enables us to directly compare our measurements in the presence of a nearly uniaxial strain with numerical calculations assuming different strain configurations. For example, Defo et al.[25] show that tensile strain in a single layer of WS_2 should lead to a 170 meV reduction in energy gap per 1% isotropic strain (i.e., 2% fractional area change). This suggests that the WS_2 regions of our HS superlattice are subjected to a fractional area change

$$\left(\frac{\Delta A}{A}\right)_{WS_2} = \frac{240}{170} \times 2\% = 2.8\% \tag{6}$$

Our FFT analysis of WS_2/WSe_2 HSs is only able to provide strain differences rather than absolute magnitudes, but by knowing the strain in WS_2 from this bandgap reduction, we can estimate the strain on the WSe_2 side of the junction from the following relationship:

$$\left(\frac{\Delta A}{A}\right)_{WS_2} - \left(\frac{\Delta A}{A}\right)_{WSe_2} = (\varepsilon_{||}(WS_2) - \varepsilon_{||}(WSe_2)) + (\varepsilon_{\perp}(WS_2) - \varepsilon_{\perp}(WSe_2)) = 3.5\% \tag{7}$$

Since $(\Delta A/A)_{WS_2} = 2.8\%$, we must have $(\Delta A/A)_{WSe_2} = -0.7\%$ (the negative sign denotes compressive strain). This level of compressive strain in single-layer WSe_2 has been predicted to have a negligible effect on the WSe_2 bandgap.[25] This is consistent with our experimental observation that the bandgap of WSe_2 in a strained coherent HS is essentially identical to the bandgap of a uniform single-layer WSe_2 van der Waals coupled to the same substrate.

The length scale over which the electronic properties of a coherent single-layer WS_2/WSe_2 HS change is likely not set by strain since that is mostly uniform but rather must be caused by some other physical mechanism. From Figure 5 we see that although there is some slight far-field band bending probably due to charge transfer, the most important length scale occurs in the near-field of the interface where the energy of the HS states changes rapidly over a distance of only ~3 nm. This is most dramatically seen by the collapse in energy of the K-point valence band edge as the interface is approached from the WSe_2 side (with little strain), but the K-point states at the conduction band edge on the WS_2 side (with uniform tensile strain) merge with Q-point states over a similar length scale. Because it cannot be explained by strain, this length scale must be electronic in nature and so is likely determined by wave function penetration from one side of the HS into the other.[13,14] Here the electronic wave function sets a natural length scale as it decays exponentially from one material to another, hybridizing with states across the interface. Such behavior has been predicted in related systems as shown in ref 26.

In conclusion, we have characterized the structural and electronic properties of a coherent single-layer WS_2/WSe_2 lateral HS. We observe atomically sharp chemical transitions at the interface and a reduction of the bandgap in WS_2 as a result of mostly uniaxial tensile strain induced by the lattice mismatch of WS_2 and WSe_2. The electronic transition at the interface occurs over a very narrow width of ~3 nm that is caused by wave function hybridization across the interface. The ability to tune the electronic properties of HS superlattices by design[27] should help pave the way for future applications involving ultrathin TMD-based electronic and optoelectronic devices.

■ ASSOCIATED CONTENT

Supporting Information

The Supporting Information is available free of charge at https://pubs.acs.org/doi/10.1021/acs.nanolett.0c04204.

Methods; ripple formation and strain relaxation; bias dependent STM; Figures S1−S5 (PDF)

■ AUTHOR INFORMATION

Corresponding Authors

Jiwoong Park − *Department of Chemistry, Pritzker School of Molecular Engineering, and James Franck Institute, University of Chicago, Chicago, Illinois 60637, United States*; Email: jwpark@uchicago.edu

Michael F. Crommie − *Department of Physics and Kavli Energy NanoScience Institute, University of California, Berkeley, California 94720, United States; Materials Sciences Division, Lawrence Berkeley Laboratory, Berkeley, California 94720, United States*; orcid.org/0000-0001-8246-3444; Email: crommie@berkeley.edu

Authors

Charlotte Herbig − *Department of Physics, University of California, Berkeley, California 94720, United States*

Canxun Zhang − *Department of Physics and Kavli Energy NanoScience Institute, University of California, Berkeley, California 94720, United States; Materials Sciences Division, Lawrence Berkeley Laboratory, Berkeley, California 94720, United States*

Fauzia Mujid − *Department of Chemistry, University of Chicago, Chicago, Illinois 60637, United States*

Saien Xie − *Pritzker School of Molecular Engineering, University of Chicago, Chicago, Illinois 60637, United States; School of Applied and Engineering Physics and Kavli Institute at Cornell for Nanoscale Science, Cornell University, Ithaca, New York 14853, United States*

Zahra Pedramrazi − *Department of Physics, University of California, Berkeley, California 94720, United States*

Complete contact information is available at:

https://dx.doi.org/10.1021/acs.nanolett.0c04204
Nano Lett. XXXX, XXX, XXX−XXX

https://pubs.acs.org/10.1021/acs.nanolett.0c04204

Notes

The authors declare no competing financial interest.

■ ACKNOWLEDGMENTS

This research was supported as part of the Center for Novel Pathways to Quantum Coherence in Materials, an Energy Frontier Research Center funded by the U.S. Department of Energy, Office of Science, Basic Energy Sciences (material growth, STM spectroscopy, dI/dV mapping). Support was also provided by the National Science Foundation through the Cornell Center for Materials Research MRSEC under Grant DMR-1719875 (coherent interface optimization) and University of Chicago MRSEC under Grant DMR-2011854 (2D material transfer), as well as through Grant DMR-1807233 (surface preparation and topographic characterization). C.H. acknowledges support from the Alexander von Humboldt Foundation for a Feodor Lynen research fellowship. F.M. acknowledges support from the National Science Foundation Graduate Research Fellowship Program under Grant DGE-1746045.

■ REFERENCES

(1) Huang, C.; Wu, S.; Sanchez, A. M.; Peters, J. J. P.; Beanland, R.; Ross, J. S.; Rivera, P.; Yao, W.; Cobden, D. H.; Xu, X. Lateral heterojunctions within monolayer MoSe2−WSe2 semiconductors. *Nat. Mater.* **2014**, *13* (12), 1096−1101.

(2) Duan, X.; Wang, C.; Shaw, J. C.; Cheng, R.; Chen, Y.; Li, H.; Wu, X.; Tang, Y.; Zhang, Q.; Pan, A.; Jiang, J.; Yu, R.; Huang, Y.; Duan, X. Lateral epitaxial growth of two-dimensional layered semiconductor heterojunctions. *Nat. Nanotechnol.* **2014**, *9* (12), 1024−1030.

(3) Li, M.-Y.; Shi, Y.; Cheng, C.-C.; Lu, L.-S.; Lin, Y.-C.; Tang, H.-L.; Tsai, M.-L.; Chu, C.-W.; Wei, K.-H.; He, J.-H.; Chang, W.-H.; Suenaga, K.; Li, L.-J. Epitaxial growth of a monolayer WSe₂-MoS₂ lateral p-n junction with an atomically sharp interface. *Science* **2015**, *349* (6247), 524.

(4) Gong, Y.; Lei, S.; Ye, G.; Li, B.; He, Y.; Keyshar, K.; Zhang, X.; Wang, Q.; Lou, J.; Liu, Z.; Vajtai, R.; Zhou, W.; Ajayan, P. M. Two-Step Growth of Two-Dimensional WSe2/MoSe2 Heterostructures. *Nano Lett.* **2015**, *15* (9), 6135−6141.

(5) Bogaert, K.; Liu, S.; Chesin, J.; Titow, D.; Gradečak, S.; Garaj, S. Diffusion-Mediated Synthesis of MoS2/WS2 Lateral Heterostructures. *Nano Lett.* **2016**, *16* (8), 5129−5134.

(6) Sahoo, P. K.; Memaran, S.; Xin, Y.; Balicas, L.; Gutiérrez, H. R. One-pot growth of two-dimensional lateral heterostructures via sequential edge-epitaxy. *Nature* **2018**, *553* (7686), 63−67.

(7) Zhang, C.; Li, M.-Y.; Tersoff, J.; Han, Y.; Su, Y.; Li, L.-J.; Muller, D. A.; Shih, C.-K. Strain distributions and their influence on electronic structures of WSe2−MoS2 laterally strained heterojunctions. *Nat. Nanotechnol.* **2018**, *13* (2), 152−158.

(8) Conley, H. J.; Wang, B.; Ziegler, J. I.; Haglund, R. F.; Pantelides, S. T.; Bolotin, K. I. Bandgap Engineering of Strained Monolayer and Bilayer MoS2. *Nano Lett.* **2013**, *13* (8), 3626−3630.

(9) Song, W.; Yang, L. Quasiparticle band gaps and optical spectra of strained monolayer transition-metal dichalcogenides. *Phys. Rev. B: Condens. Matter Mater. Phys.* **2017**, *96* (23), 235441.

(10) Xie, S.; Tu, L.; Han, Y.; Huang, L.; Kang, K.; Lao, K. U.; Poddar, P.; Park, C.; Muller, D. A.; DiStasio, R. A.; Park, J. Coherent, atomically thin transition-metal dichalcogenide superlattices with engineered strain. *Science* **2018**, *359* (6380), 1131.

(11) Koo, E.; Lee, Y.; Song, Y.; Park, M.; Ju, S.-Y. Growth Order-Dependent Strain Variations of Lateral Transition Metal Dichalcogenide Heterostructures. *ACS Applied Electronic Materials* **2019**, *1* (1), 113−121.

(12) Chu, Y.-H.; Wang, L.-H.; Lee, S.-Y.; Chen, H.-J.; Yang, P.-Y.; Butler, C. J.; Lu, L.-S.; Yeh, H.; Chang, W.-H.; Lin, M.-T. Atomic scale depletion region at one dimensional MoSe2-WSe2 heterointerface. *Appl. Phys. Lett.* **2018**, *113* (24), 241601.

(13) Cobley, R. J.; Teng, K. S.; Maffeïs, T. G. G.; Wilks, S. P. Cross-sectional scanning tunneling microscopy and spectroscopy of strain in buried heterostructure lasers. *Surf. Sci.* **2006**, *600* (14), 2857−2859.

(14) Cobley, R. J.; Rees, P.; Teng, K. S.; Wilks, S. P. Analyzing real-time surface modification of operating semiconductor laser diodes using cross-sectional scanning tunneling microscopy. *J. Appl. Phys.* **2010**, *107* (9), No. 094507.

(15) Ugeda, M. M.; Bradley, A. J.; Shi, S.-F.; da Jornada, F. H.; Zhang, Y.; Qiu, D. Y.; Ruan, W.; Mo, S.-K.; Hussain, Z.; Shen, Z.-X.; Wang, F.; Louie, S. G.; Crommie, M. F. Giant bandgap renormalization and excitonic effects in a monolayer transition metal dichalcogenide semiconductor. *Nat. Mater.* **2014**, *13* (12), 1091−1095.

(16) Zhang, Y.; Ugeda, M. M.; Jin, C.; Shi, S.-F.; Bradley, A. J.; Martín-Recio, A.; Ryu, H.; Kim, J.; Tang, S.; Kim, Y.; Zhou, B.; Hwang, C.; Chen, Y.; Wang, F.; Crommie, M. F.; Hussain, Z.; Shen, Z.-X.; Mo, S.-K. Electronic Structure, Surface Doping, and Optical Response in Epitaxial WSe2 Thin Films. *Nano Lett.* **2016**, *16* (4), 2485−2491.

(17) Hill, H. M.; Rigosi, A. F.; Rim, K. T.; Flynn, G. W.; Heinz, T. F. Band Alignment in MoS2/WS2 Transition Metal Dichalcogenide Heterostructures Probed by Scanning Tunneling Microscopy and Spectroscopy. *Nano Lett.* **2016**, *16* (8), 4831−4837.

(18) Huang, Y. L.; Ding, Z.; Zhang, W.; Chang, Y.-H.; Shi, Y.; Li, L.-J.; Song, Z.; Zheng, Y. J.; Chi, D.; Quek, S. Y.; Wee, A. T. S. Gap States at Low-Angle Grain Boundaries in Monolayer Tungsten Diselenide. *Nano Lett.* **2016**, *16* (6), 3682−3688.

(19) Ugeda, M. M.; Pulkin, A.; Tang, S.; Ryu, H.; Wu, Q.; Zhang, Y.; Wong, D.; Pedramrazi, Z.; Martín-Recio, A.; Chen, Y.; Wang, F.; Shen, Z.-X.; Mo, S.-K.; Yazyev, O. V.; Crommie, M. F. Observation of topologically protected states at crystalline phase boundaries in single-layer WSe2. *Nat. Commun.* **2018**, *9* (1), 3401.

(20) Zhang, C.; Chen, Y.; Johnson, A.; Li, M.-Y.; Li, L.-J.; Mende, P. C.; Feenstra, R. M.; Shih, C.-K. Probing Critical Point Energies of Transition Metal Dichalcogenides: Surprising Indirect Gap of Single Layer WSe2. *Nano Lett.* **2015**, *15* (10), 6494−6500.

(21) Manzeli, S.; Ovchinnikov, D.; Pasquier, D.; Yazyev, O. V.; Kis, A. 2D transition metal dichalcogenides. *Nat. Rev. Mater.* **2017**, *2* (8), 17033.

(22) Zhang, C.; Johnson, A.; Hsu, C.-L.; Li, L.-J.; Shih, C.-K. Direct Imaging of Band Profile in Single Layer MoS2 on Graphite: Quasiparticle Energy Gap, Metallic Edge States, and Edge Band Bending. *Nano Lett.* **2014**, *14* (5), 2443−2447.

(23) Huang, Y. L.; Chen, Y.; Zhang, W.; Quek, S. Y.; Chen, C.-H.; Li, L.-J.; Hsu, W.-T.; Chang, W.-H.; Zheng, Y. J.; Chen, W.; Wee, A. T. S. Bandgap tunability at single-layer molybdenum disulphide grain boundaries. *Nat. Commun.* **2015**, *6* (1), 6298.

(24) Sung, J. H.; Heo, H.; Si, S.; Kim, Y. H.; Noh, H. R.; Song, K.; Kim, J.; Lee, C.-S.; Seo, S.-Y.; Kim, D.-H.; Kim, H. K.; Yeom, H. W.; Kim, T.-H.; Choi, S.-Y.; Kim, J. S.; Jo, M.-H. Coplanar semiconductor−metal circuitry defined on few-layer MoTe2 via polymorphic heteroepitaxy. *Nat. Nanotechnol.* **2017**, *12* (11), 1064−1070.

(25) Defo, R. K.; Fang, S.; Shirodkar, S. N.; Tritsaris, G. A.; Dimoulas, A.; Kaxiras, E. Strain dependence of band gaps and exciton energies in pure and mixed transition-metal dichalcogenides. *Phys. Rev. B: Condens. Matter Mater. Phys.* **2016**, *94* (15), 155310.

(26) Wei, W.; Dai, Y.; Huang, B. Straintronics in two-dimensional in-plane heterostructures of transition-metal dichalcogenides. *Phys. Chem. Chem. Phys.* **2017**, *19* (1), 663−672.

(27) Sarkar, D.; Xie, X.; Liu, W.; Cao, W.; Kang, J.; Gong, Y.; Kraemer, S.; Ajayan, P. M.; Banerjee, K. A subthermionic tunnel field-effect transistor with an atomically thin channel. *Nature* **2015**, *526* (7571), 91−95.

https://dx.doi.org/10.1021/acs.nanolett.0c04204
Nano Lett. XXXX, XXX, XXX−XXX